PNAS RESEARCH ARTICLE | PHYSICS

Magnetochiral tunneling in paramagnetic $Co_{1/3}NbS_2$

Seongjoon Lim[a,1], Sobhit Singh[b,c,1], Fei-Ting Huang[a], Shangke Pan[a,d], Kefeng Wang[a], Jaewook Kim[a], Jinwoong Kim[e], David Vanderbilt[e,2], and Sang-Wook Cheong[a,2]

Contributed by David Vanderbilt; received October 24, 2023; accepted January 25, 2024; reviewed by Silvia Picozzi and Peter Wahl

Electric currents have the intriguing ability to induce magnetization in nonmagnetic crystals with sufficiently low crystallographic symmetry. Some associated phenomena include the non-linear anomalous Hall effect in polar crystals and the nonreciprocal directional dichroism in chiral crystals when magnetic fields are applied. In this work, we demonstrate that the same underlying physics is also manifested in the electronic tunneling process between the surface of a nonmagnetic chiral material and a magnetized scanning probe. In the paramagnetic but chiral metallic compound $Co_{1/3}NbS_2$, the magnetization induced by the tunneling current is shown to become detectable by its coupling to the magnetization of the tip itself. This results in a contrast across different chiral domains, achieving atomic-scale spatial resolution of structural chirality. To support the proposed mechanism, we used first-principles theory to compute the chirality-dependent current-induced magnetization and Berry curvature in the bulk of the material. Our demonstration of this magnetochiral tunneling effect opens up an avenue for investigating atomic-scale variations in the local crystallographic symmetry and electronic structure across the structural domain boundaries of low-symmetry nonmagnetic crystals.

Berry curvature dipole | spin-polarized scanning tunneling microscopy | two-dimensional materials

Significance

The appearance of a magnetic signal in scanning tunneling microscopy (STM) is usually attributed to the relative magnetizations of tip and sample. Here we show that it can arise instead from a broken crystallographic symmetry in a nonmagnetic sample. In particular, we show that domains of opposite handedness can be distinguished at the surface of the chiral compound $Co_{1/3}NbS_2$, despite the fact that these are nonmagnetic. We attribute this signal to a magnetization induced in the sample by the tunneling current, a mechanism that is facilitated by an asymmetric distribution of Berry curvature in reciprocal space. Our work opens opportunities for using magnetic STM to provide high-resolution images of nonmagnetic domain structures associated with purely crystallographic broken symmetries.

Since its invention, scanning tunneling microscopy (STM) has had a profound impact on the fields of nanotechnology and materials science due to its unique ability to achieve atomic-scale spatial and meV energy resolution and to manipulate atoms (1). Its magnetic variant, spin-polarized scanning tunneling microscopy (SP-STM), which makes use of magnetized probes, has been particularly useful in the study of atomic-scale magnetic order (2). Notably, SP-STM has been extensively used to explore such novel phenomena as Majorana zero modes (3) and single-molecule magnets (4). However, to date, the application of SP-STM has primarily been limited to the study of spontaneous long-range magnetic order in the sample, since it relies on distinct tunneling probabilities for parallel and antiparallel magnetizations between probe and sample (2).

The recent discovery of current-induced bulk magnetization in nonmagnetic chiral structures (5–10) has prompted us to consider the feasibility of observing current-induced magnetization through the application of SP-STM. While tunneling currents are small, they become highly concentrated in the sample just below the tip, so that the magnetic detection of nonmagnetic domains with opposite chiralities at a crystal surface becomes plausible. Such an application of SP-STM promises to provide enormously improved resolution for imaging of chiral domain structures compared to diffraction-limited optical techniques.

Moreover, the phenomenon of current-induced bulk magnetization, known as the kinetic magnetoelectric effect, has been investigated theoretically (11–15) and shown to be closely related to some unconventional quantum responses such as nonlinear anomalous Hall (16–20), second harmonic transport (21), kinetic Faraday (12, 22), gyrotropic magnetic (11), and circular photogalvanic (12) effects, as well as the Edelstein effect in 2D (23). These have been shown to be governed by quantum geometric effects associated with the presence of Berry curvature in the electronic band structure of acentric crystals even without broken time-reversal symmetry. In particular, there has been considerable recent interest in the so-called "Berry curvature dipole" (BCD), which describes an imbalance of Berry curvature in the Brillouin zone and governs the nonlinear anomalous Hall effect (17, 19, 24–26). Theory indicates an intimate connection between the current-induced spin and orbital magnetization and nonlinear Hall effects, which also have very similar broken symmetry requirements and typically appear together in chiral crystals (24, 25, 27). In fact, these properties can be used as a probe of broken spatial symmetries arising from chiral, polar, ferro-rotational, or other structural orders, based either on conventional symmetry analysis or in the framework of symmetry operational similarity (28). They offer an intriguing opportunity to explore the emergence of quantum phenomena arising from Berry curvature, especially those associated with topological features of the band

Author contributions: D.V. and S.-W.C. designed research; S.L., S.S., F.-T.H., S.P., K.W., Jaewook Kim, and Jinwoong Kim performed research; S.L. performed STM and analyzed data; S.S. carried out theoretical calculations; F.-T.H. performed TEM imaging; S.P. and K.W. grew crystals; Jaewook Kim carried out magnetic susceptibility measurements; Jinwoong Kim assisted with theoretical calculations; D.V. initiated and supervised theoretical calculations; S.-W.C. conceived the project; and S.L., S.S., D.V., and S.-W.C. wrote the paper.

Reviewers: S.P., Consiglio Nazionale delle Ricerche - SuPerconducting and other INnovative materials and devices institute; and P.W., University of St. Andrews.

The authors declare no competing interest.

[1]S.L. and S.S. contributed equally to this work.

[2]To whom correspondence may be addressed. Email: dhv@physics.rutgers.edu or sangc@physics.rutgers.edu.

This article contains supporting information online at https://www.pnas.org/lookup/suppl/doi:10.1073/pnas.2318443121/-/DCSupplemental.

Published February 27, 2024.

structure (13), at the atomic scale if they can be coupled to a local magnetic probe such as a scanning tip.

In this work, we demonstrate the proposed SP-STM detection of current-induced magnetization to reveal crystallographic chirality in nonmagnetic substrates. Specifically, we show that $Co_{1/3}NbS_2$, a structurally chiral material in a nonmagnetic state, can host a type of kinetic magnetoelectric effect in which an electric current tunneling out of the surface and into the tip carries a detectable magnetization, providing a contrast mechanism for mapping chiral domain structures. We will use the term "magnetochiral tunneling effect" (MTE) for this magnetoelectric phenomenon. Our symmetry considerations and first-principles calculations of the uniform bulk current-induced spin and orbital magnetizations and BCD provide support for the conclusion that the observed magnetic signal is, indeed, caused by these phenomena operating in the region of high current density concentrated under the scanning tip. This finding provides a mechanism for the direct determination of crystallographic chirality at the atomic scale, highlights the role of electronic Berry curvature and opens the possibility of studying other types of broken crystallographic symmetries using a similar approach.

Results

In order to detect the MTE, we choose a class of layered two-dimensional chiral metals, $M_{1/3}(Nb,Ta)S_2$ (M=3*d* transition metals), which have attracted significant interest due to the structural chiral domains outlined by a network of vortex and anti-vortex pairs (29–31). The sub-micron-scale chiral domains and boundaries that comprise the heterochiral structure in $M_{1/3}(Nb,Ta)S_2$ provide a unique platform for observing the influence of quantum geometric effects on the opposite structural chiralities. Additionally, $Cr_{1/3}NbS_2$, one of the isostructural materials with helical magnetism, has been reported to show chirality-induced magnetic transport (9). Therefore, even in the absence of magnetic order, it might be possible to find a similar chirality-induced magnetoelectric interaction in an isostructural member. Focusing on $Co_{1/3}NbS_2$, we use SP-STM to detect the change in the magnetic signal produced by the magnetoelectric interaction across a chiral domain boundary at the atomic scale. We further elucidate the origin of the observed magnetic signal across the chiral domain boundary based on first-principles density-functional theory (DFT) calculations that demonstrate the appearance of non-vanishing magnetization and net Berry curvature under a quasi-equilibrium flow of electric current.

Symmetry Considerations. First, we examine the symmetry operational (28, 32) properties of various components related to MTE or the current-induced magnetization (5, 9, 33, 34) in the bulk chiral structure. Fig. 1*A* illustrates that the presence of a mirror plane parallel to the electric current switches the chirality (green helix) as well as the sign of the induced magnetization (blue arrow), while the electric current (orange arrow) remains unchanged. On the other hand, a two-fold rotation (C_2) around an axis perpendicular to the current reverses only the magnetization and the current, not the chirality. This relationship, reminiscent of a magnetic field induced by a current flowing around a coil, can also be examined in reciprocal space in relation to Berry curvature (Fig. 1*B*). In the presence of an electric current (orange arrows), the Berry curvature (small light-blue arrows) along the direction of the flow determines the induced magnetization (blue arrows). The Berry curvature and magnetization, being pseudo-vectorial quantities, change sign under the mirror operation. Instead, application of a C_2 rotation around an axis perpendicular to the current flips the electric current direction and the induced magnetization, while the texture of the Berry curvature remains unchanged. Therefore, the symmetry analysis predicts that the current-induced MTE should be reversible by two factors: structural chirality and electric current direction (28, 32). Further analysis based on symmetry operational similarity suggests that other types of spatial symmetries, such as polar structures, can also exhibit similar coupling between electric current and the broken lattice symmetry. We provide more details in *SI Appendix*, Note 1.

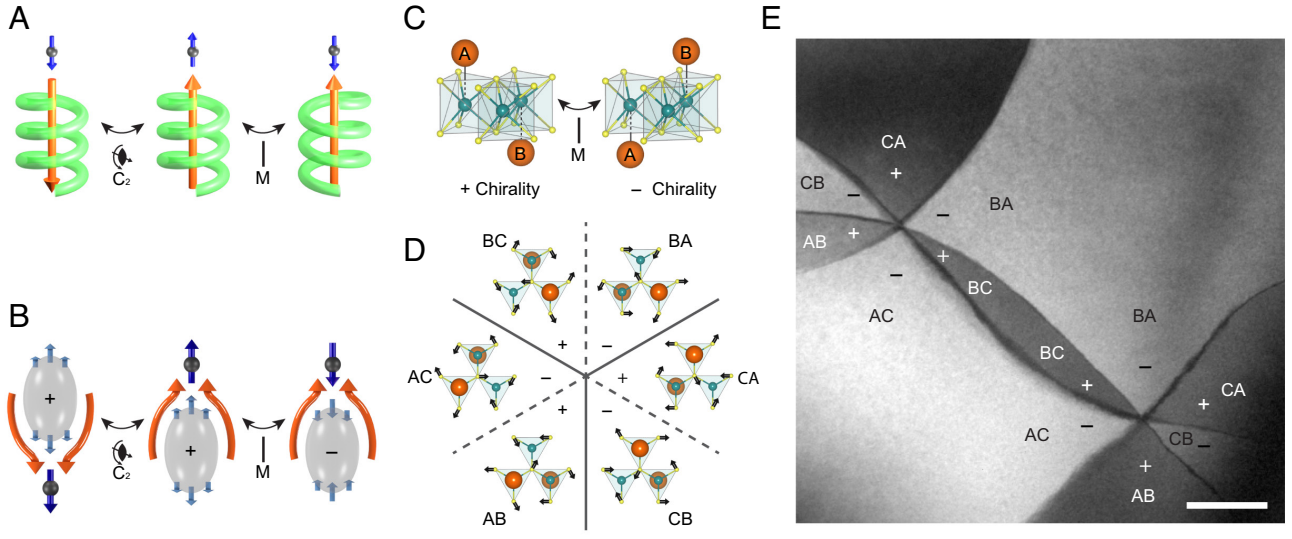

Fig. 1. Mirror symmetry operation on (pseudo) vectors and chiral structures. (*A* and *B*) Changes of (pseudo) vectorial quantities under C_2 and mirror operations in real (*A*) and reciprocal (B) space. Chiral structure (green helix), electric current (orange arrow), magnetization (blue arrow), and Berry curvature (small light-blue arrow) are transformed by mirror operation (*Right*) and C_2 rotation (*Left*) from the reference (*Center*). The structural chirality is indicated by + and – signs in (*B*). (*C*) Two chiralities (+ and –) in the chiral layered compound $Co_{1/3}NbS_2$ are connected by a mirror symmetry operation. The alternation of the intercalant sites of Co atoms (orange) along the *c* axis gives AB and BA type structures with opposite chirality. (*D*) Six configurations of antiphase domains with alternating structural chirality around a vortex. Solid (dashed) line indicates a change of Co lattice above (below) the NbS_2 layer. (*E*) Topological vortex and antivortex pair with six domains observed with transmission electron microscopy. The dark and bright contrast reveals the structural chirality as indicated by + and – signs, respectively. (Scale bar, 0.5μm.)

STM/SP-STM Results. The structure of $Co_{1/3}NbS_2$ depicted in Fig. 1*C* is formed through the intercalation of Co ions into the van der Waals gap of the centrosymmetric parent material 2H-NbS_2. The structure belongs to one of the 65 Sohncke groups (SG#182, $P6_322$) that can exhibit opposite chiral structures within the same space group (35). The Co ions within a van der Waals gap occupy one of the three Nb-atop sites, which are labeled A, B, and C. The intercalation sites in adjacent gaps along the *c* direction alternate between two sites. Since only two of the three Nb-atom sites are occupied, there are six permutation pairs (*i.e.* AB, BC, CA, BA, CB, and AC). The six pairs form two kinds of structural chiralities, which we designate as + and – chirality (30). Within each chirality, there are three structures that are mutually convertible by C_3 rotation (AB, BC, and CA for + chirality; BA, CB, and AC for – chirality). The formation of a topological vortex showing alternating chiral domains is described in Fig. 1*D*, and the real-space observation using dark-field transmission electron microscopy is shown in Fig. 1*E*. The present result of a topological vortex in $Co_{1/3}NbS_2$ is consistent with previous observations of topological vortex formation in the isostructural $M_{1/3}TaS_2$ compounds (29, 30, 36). We note that there are two types of boundaries depending on the Co layer in which the lattice shifts, which are depicted in Fig. 1*D* with solid and dashed lines. The boundaries with solid lines, which involve a change in the first character (e.g. AB to CB), are accompanied by a change in the intercalation site in the upper Co lattice (i.e. the exposed Co lattice on a surface). The boundaries with dashed lines (e.g. CB to CA) involve a change in the lower Co lattice (i.e., the Co underneath the NbS_2 layer).

We cleave samples for STM and SP-STM at a cleaving stage with liquid nitrogen cooling (31, 37) and all measurements are carried out at 78K to avoid the antiferromagnetic ordering, which occurs below 29K (38–40) (*SI Appendix*, Fig. S3 for susceptibility measurement). We adopt liquid nitrogen cooling to achieve optimal thermal stability at a temperature above the antiferromagnetic order. While it constrains the use of helium-cooled superconducting coil, the extended holding time of liquid nitrogen facilitates the consistent application of the lateral coarse-moving mechanism of the STM setup until a topological vortex is pinpointed. On cleaved surfaces, we could identify two types of surfaces that expose Co and NbS_2 on the top surface (*SI Appendix*, Fig. S5), and only Co-type surfaces are adopted in this study. The topographies in Fig. 2 *A* and *B* highlight the observation of a topological vortex in STM and SP-STM, respectively. The STM result clearly reveals the three domain boundaries connected to the vortex despite the presence of various atomic defects such as Co ions in a metastable charge state (bright spots) and Co vacancies (dark spots), which we have identified in our previous study (31). On the other hand, SP-STM on the same surface region reveals an additional two-level domain contrast around the vortex, with the contrast being more pronounced in a larger-scale image due to averaging out of randomly distributed atomic defects (Fig. 2*B*, *Inset*).

To understand the appearance of only three domain boundaries instead of six in the STM image, we set up two atomic models of the chiral domain boundaries as shown in Fig. 1*D* based on our previous study (30). Fig. 2 *F* and *G* show the models with a shift in the Co lattice above and underneath the NbS_2 layer, respectively. The difference is that Fig. 2*F* has a shift of the surface Co lattice (circles with solid lines) by 1/3 of the unit cell size, while Fig. 2*G* does not. Analysis of the STM image (Fig. 2*C*) shows that the three domain boundaries in the STM image belong to the type shown in Fig. 2*F*. The other three boundaries underneath could not be located within the bias range of a few hundreds of mV, and use of higher bias voltage is limited by the presence of metastable charge states of Co ions (31).

In stark contrast to the STM results, the two-level domain contrast appears in the SP-STM image, facilitating the identification of all six chiral domains and boundaries. Among the six chiral domain boundaries, only three of them showed a shift of Co lattice (Fig. 2*D*) similar to the STM result. The other three boundaries, on the other hand, do not show a shift (Fig. 2*E*), which is consistent with the second type domain boundary (Fig. 2*G*). Instead, there exists a stepwise change in topography as shown in Fig. 2*H*. Because the contrast is only observed when using a magnetized probe, we assign the signal to be magnetic suggesting that it is related to a magnetoelectric interaction with the structural chirality. We exclude the possibility that this two-level contrast originates from a long-range order of Co spins, as the measurement temperature (78K) is well above the antiferromagnetic transition temperature (29K) (38–40). Furthermore, the two-level domain contrast that is locked to the structural chirality is not consistent with the stripe pattern expected from the antiferromagnetic order (41). Thus, we explore the possibility that the magnetic two-level contrast is related to the MTE that can occur in chiral structures (5, 6, 10, 12, 15, 33, 42), using the formalism of gyrotropic magnetoelectric and BCD effects in the electronic structure (19, 24, 26, 43) as we explain next.

Theoretical Analysis. We use density-functional theory (DFT+U) calculations with spin–orbit coupling (SOC) to analyze the electronic band structure of the two inverted bulk chiral structures of $Co_{1/3}NbS_2$. We carry out DFT+U+SOC calculations (*Materials and Methods*) for ferromagnetic, antiferromagnetic, and nonmagnetic configurations (*SI Appendix*, Note 9), obtaining a metallic ground state with a complex Fermi surface dominated by Nb *d*, Co *d*, and S *p* orbitals in all cases. Since the material is paramagnetic at the experimental conditions, we focus henceforth on the nonmagnetic case, for which the band structure is shown in Fig. 3*A*. For consistency, we continue to use DFT+U (44), although the Hubbard *U* has very little effect on the nonmagnetic calculation (*SI Appendix*, Note 10).

To better understand how a current flowing along the *z* symmetry axis of $Co_{1/3}NbS_2$ activates the appearance of a corresponding *z* magnetization, we examine the *z* components of the spin (S_z) and Berry curvature ($\mathbf{\Omega}_z$) in reciprocal space. Fig. 3*B* shows the expectation value of S_z for bands along the Γ-A (k_z) high-symmetry direction of the Brillouin zone (BZ) for both chiral variants. Fig. 3*C* presents S_z projected onto the Fermi surface, while 3D shows S_z projected onto the Fermi loops on a k_x-k_z plane at k_y=0. We confirm that both S_z and $\mathbf{\Omega}_z$ change sign upon chirality reversal. We also note that they reverse sign under $\mathbf{k} \rightarrow -\mathbf{k}$ in reciprocal space, i.e., $\mathbf{\Omega}_z(\mathbf{k})=-\mathbf{\Omega}_z(\mathbf{k})$ and $S_z(\mathbf{k})=-S_z(\mathbf{k})$, as expected from time-reversal symmetry. Symmetry considerations imply that all three pseudovectors $S_z(\mathbf{k})$, $\mathbf{\Omega}_z(\mathbf{k})$, and $L_z(\mathbf{k})$ follow the same symmetry rules. Each of these quantities integrates to zero over the occupied Fermi sea at equilibrium but becomes non-zero because of the imbalanced occupation that results from a flow of electric current along *z* as schematically shown in Fig. 4 *A* and *B* (7, 19). This is shown for the Berry curvature in Fig. 3*C*, where the green arrows indicate the direction of the BCD, but the same applies to the generation of magnetization. Since we do not know the details of the tunneling process from sample to tip, we remain open to the possibility that all of these induced quantities—spin, orbital moment, and Berry curvature—could contribute in different ways.

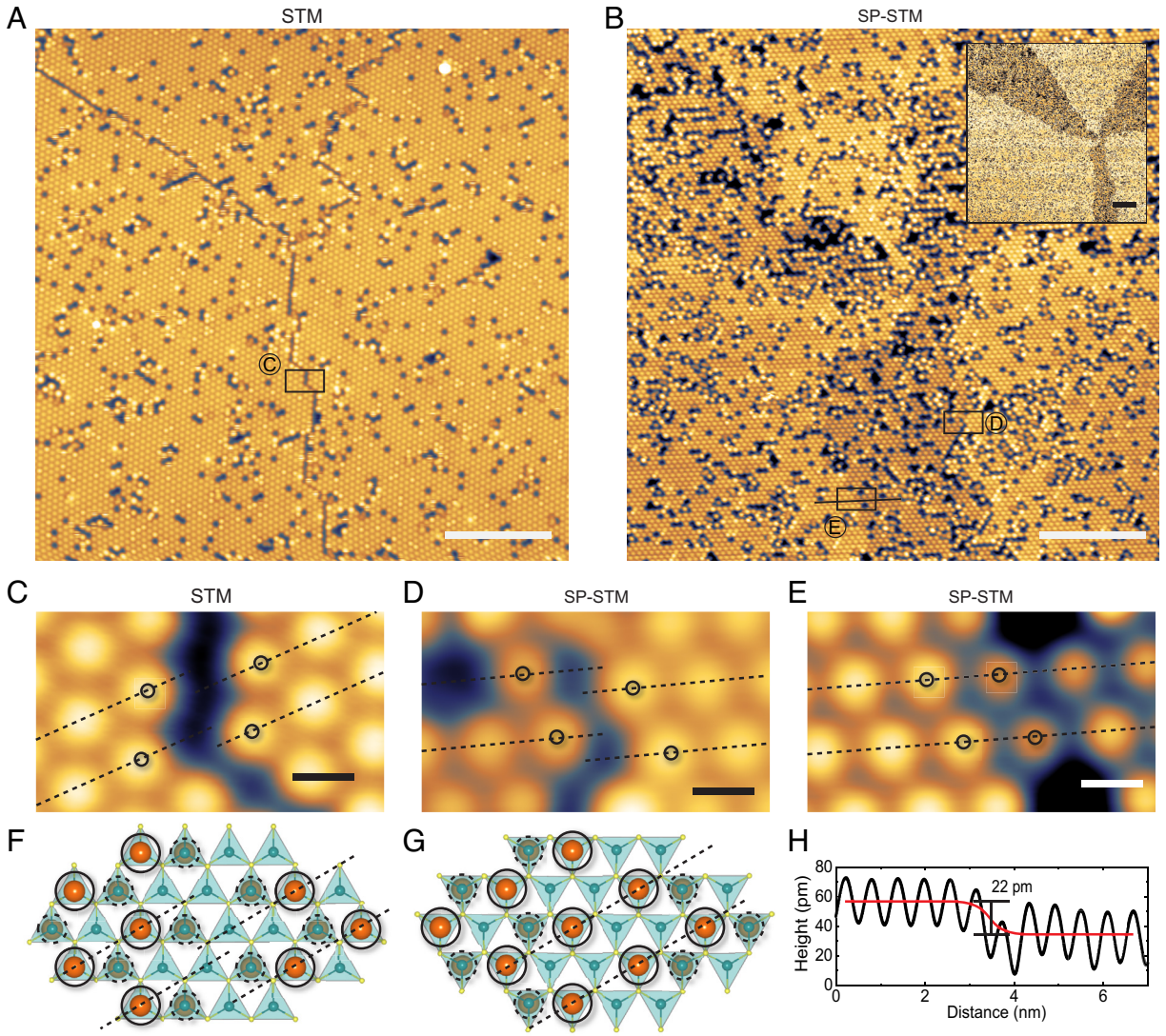

Fig. 2. STM and SP-STM observation of chiral domains around a vortex. (*A*) STM topography shows only three domain boundaries around the topological vortex at the center (5mV, 5 pA). (Scale bar, 10nm.) (*B*) SP-STM observation reveals all of six domains by alternating domain contrast. The two-level contrast is more evident in the large-area image in the *Inset* (−50mV, 10 pA). (Scale bar, 10nm; Inset, 20nm.) (*C* and *D*) Domain boundaries with a shift of the Co lattice on top of the NbS_2 layer can be observed in STM (*C*) and SP-STM (*D*). The dashed lines show a shift of 1/3 of the unit cell. (*E*) Domain boundaries without a shift of the Co lattice can only be observed in SP-STM. The dashed lines show no shift of the Co lattice. (Scale bars, 0.7nm.) (*F*) Atomic model of a domain boundary with Co lattice shift above the NbS_2 layer that corresponds to (*C*) and (*D*). (*G*) Atomic model of a domain boundary with the Co lattice shift underneath the NbS_2 layer that corresponds to (*E*). (*H*) Domain contrast across the domain boundary in SP-STM. The height profile is obtained along the black line in (*B*) and reveals 22pm of step-like change across the boundary. The red line is a guide to the eye.

To be specific, we compute the two kinetic magnetoelectric tensors $K^{\rm spin}$ and $K^{\rm orb}$ and the BCD tensor D defined by:

$$K_{ij}^{\rm spin} = \sum_n \frac{1}{(2\pi)^3} \int d^3k f_{n\mathbf{k}} \frac{\partial}{\partial k_j} m_{n\mathbf{k},i}^{\rm spin}, \quad [1]$$

$$K_{ij}^{\rm orb} = \sum_n \frac{1}{(2\pi)^3} \int d^3k f_{n\mathbf{k}} \frac{\partial}{\partial k_j} m_{n\mathbf{k},i}^{\rm orb}, \quad [2]$$

$$D_{ij} = \sum_n \frac{1}{(2\pi)^3} \int d^3k f_{n\mathbf{k}} \frac{\partial}{\partial k_j} \Omega_{n\boldsymbol{k},i}. \quad [3]$$

These equations describe the spin magnetization, orbital magnetization, and integrated Berry curvature induced by a uniform displacement of the Fermi surface along direction j, where $m_{n\mathbf{k},i}^{\rm spin}$ and $m_{n\mathbf{k},i}^{\rm orb}$ are the $i^{\rm th}$ components of the spin and orbital moments of the Bloch state of band n at wavevector $\mathbf{k}$ with occupation $f_{n\mathbf{k}}$, and $\boldsymbol{\Omega}_{n\boldsymbol{k},i}$ is the corresponding Berry curvature. The responses to a static uniform electric field E_j in the limit of a constant relaxation time τ are given by $M_i = \chi_{ij} E_j$ with $\chi_{ij}^{\rm spin} = (-e\tau/\hbar) K_{ij}^{\rm spin}$ and $\chi_{ij}^{\rm orb} = (-e\tau/\hbar) K_{ij}^{\rm orb}$, while the nonlinear Hall effect is described by an induced current $j_i = \chi_{ijk}^{\rm NLH} E_j E_k$ with $\chi_{ijk}^{\rm NLH} = \left(-e^3\tau/2\right)\epsilon_{ilk} D_{jl}$, in implied sum notation (e>0 is the charge quantum, and $\hbar$ is the reduced Planck's constant).

Under the D_6 point group, the kinetic magnetic tensors have components $K_{xx} = K_{yy}$ and K_{zz} as the only allowed non-zero elements, while in addition, $D_{xx} = D_{yy} = -D_{zz}/2$ for the special case of the BCD (12). It is straightforward to show that these tensors transform in the usual way under proper crystal symmetry operations but

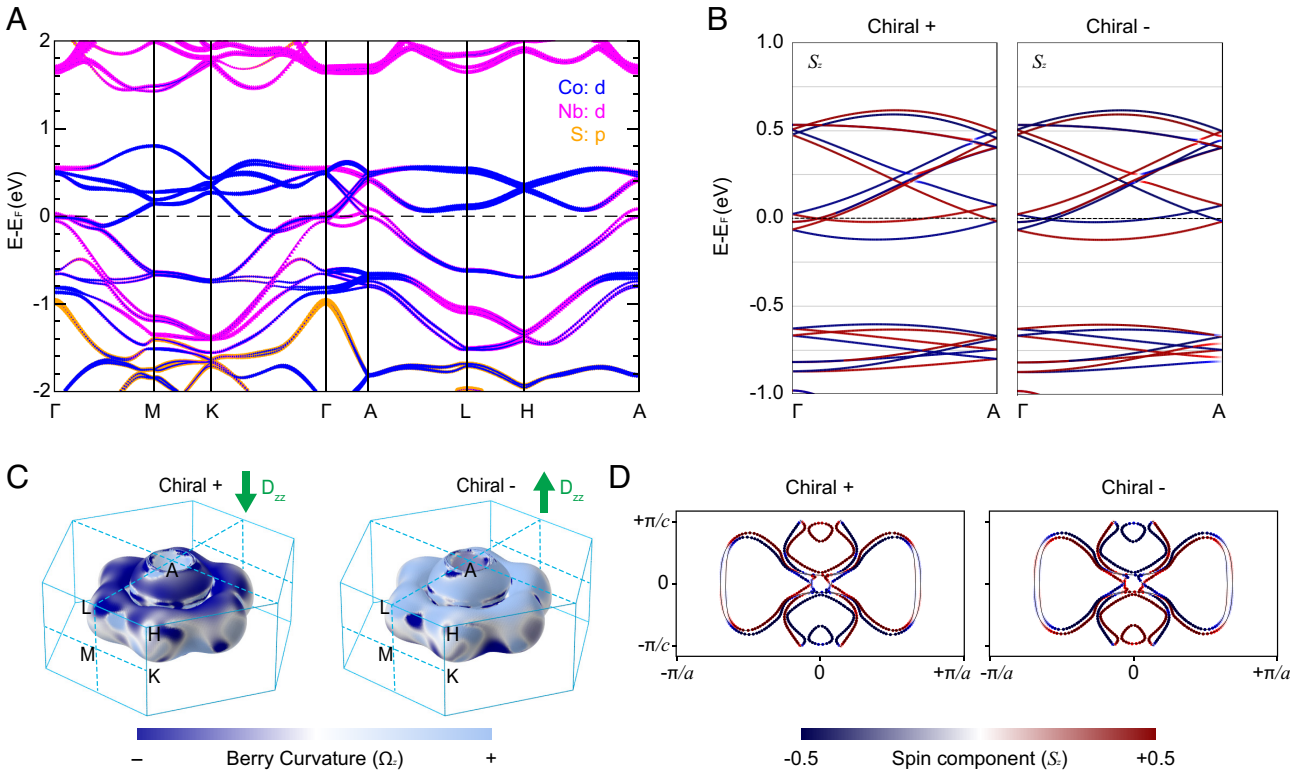

Fig. 3. Electronic band structure, spin texture, and Berry curvature. (*A*) Atomic-orbital resolved electronic band structure calculated with inclusion of SOC for non-magnetic $Co_{1/3}NbS_2$. (*B*) S_z component of spin magnetization projected on the electronic band structure along the high-symmetry k_z direction of the BZ for + and – chiral structures. Dashed horizontal line depicts the Fermi level. Red and blue colors denote the positive and negative values of S_z, respectively. (*C*) Color-mapped distribution of the *z* component of Berry curvature Ω_z on the Fermi surface from both chiral structures. The direction of D_{zz} ($\propto \frac{\partial \tilde{\Omega}_z}{\partial k_z}$) is indicated by green arrows. (*D*) Spin texture S_z of both chiral structures calculated in the k_y= 0 plane (i.e., the k_x–k_z plane) in the full BZ.

acquire an extra minus sign under improper ones, thus explaining the sign reversal for the case of opposite chiral domains.

Since experimentally our surface is normal to *z* and the tip bias generates an electric field that is dominantly along *z* in the region just below the STM tip, we now focus on computing the *zz* components of these tensors. In practice, we use the Fermi-surface formulation obtained from an integration by parts on Eqs. **1**–**3**, i.e.,

$$K_{zz}^{\text{spin}}(E_F) = \sum_n \frac{1}{(2\pi)^3} \int d^3k \frac{\partial E_{n,\boldsymbol{k}}}{\partial k_z} m_{n\boldsymbol{k},z}^{\text{spin}} \delta(E_{n\boldsymbol{k}} - E_F), \qquad [4]$$

and similarly for K_{zz}^{orb} and D_{zz} (11, 12). We also consider variations of E_F in these equations as describing, in a rigid-band approximation, variable bias voltages that may be applied in the tunneling experiments.

In Fig. 4*C* (*Upper*), we plot the variation of K_{zz}^{orb} and K_{zz}^{spin} calculated as a function of the chemical potential relative to the Fermi energy. Our calculations reveal that the K_{zz}^{orb} contribution in $Co_{1/3}NbS_2$ is about two orders of magnitude larger than the K_{zz}^{spin} contribution. This is consistent with the weakness of SOC in this compound and the fact that K_{zz}^{spin} would vanish in the absence of SOC while K_{zz}^{orb} (and the BCD) would not. This is the reverse of the usual situation in static magnetic compounds, where spin effects typically dominate; the difference here is that the tunneling current, which drives these effects, is itself orbital in nature. We observe that both the K_{zz}^{spin} and K_{zz}^{orb} as well as D_{zz} (*SI Appendix*, Fig. S12) reverse their sign upon the chirality reversal. Consequently, the current-induced magnetization resulting from these quantities will also reverse its direction, in agreement with our experimental findings.

Going one step further, we estimate the magnitude of the current-induced magnetization using the calculated spin and orbital K_{zz} data. We find it convenient to introduce the tensors $\tilde{\chi}_{ij}^{\text{spin}} = dM_i^{\text{spin}}/dJ_j$ and $\tilde{\chi}_{ij}^{\text{orb}} = dM_i^{\text{orb}}/dJ_j$, which have units of length and characterize the magnetizations in directions *i* induced per unit current along *j*. Making use of the Ohmic conductivity $\sigma_{ij}=dJ_i/dE_j$ and taking note of the presence of the symmetry axis, it follows that $\tilde{\chi}_{zz}^{\text{spin}} = \frac{\chi_{zz}^{\text{spin}}}{\sigma_{zz}} = \left(\frac{-e\tau}{\hbar}\sigma_{zz}\right) K_{zz}^{\text{spin}}$, and similarly for $\tilde{\chi}_{ij}^{\text{orb}}$. We illustrate the variation of $\tilde{\chi}_{zz}$ as a function of the chemical potential near the Fermi energy in Fig. 4 *C* (*Lower*). At the Fermi energy, we find $\tilde{\chi}_{zz}^{\text{orb}}$=–0.7 Å, whereas $\tilde{\chi}_{zz}^{\text{spin}} = 0.002$ Å. The relatively small value of the latter (and of K_{zz}^{spin}) is due to the moderate SOC of the constituent elements in $Co_{1/3}NbS_2$.

In addition, we evaluate the total bias-dependent magnetization density M_z by taking the experimentally measured J_z at each bias voltage and multiplying by the $\tilde{\chi}_{zz}^{\text{total}}$ computed at that bias. The results are plotted in Fig. 4*D* after converting units from A/cm to μ_B/cell. The maximum estimated $|M_z|$ is about 3×10^{-3} μ_B/cell at a bias voltage of –50 mV. We note that the same order of magnitude of current-induced M_z response has been experimentally observed in the isostructural chiral compound $Cr_{1/3}NbS_2$ by SQUID magnetometry (8). The derivation and calculation of $\tilde{\chi}_{zz}$ along with the theoretical assessment of

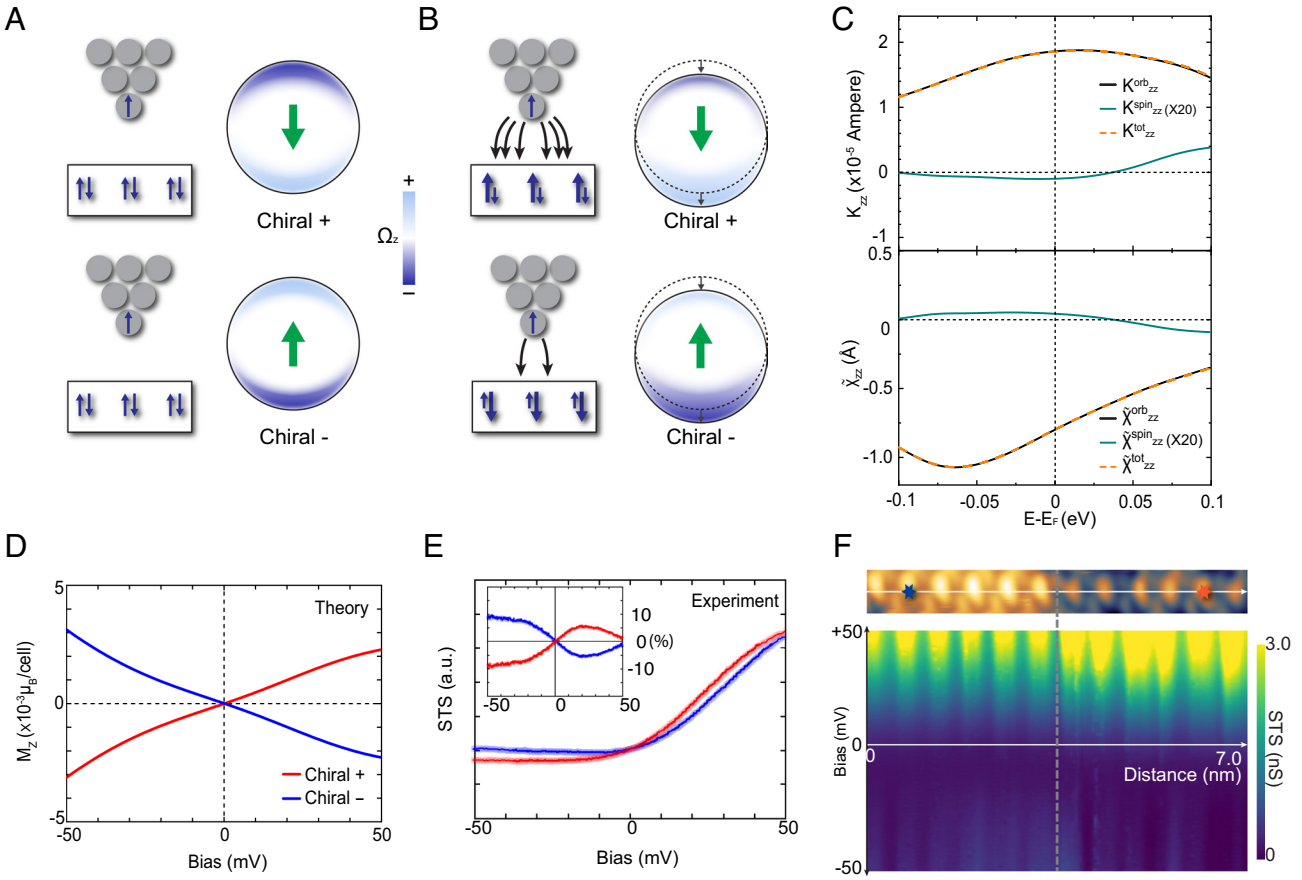

Fig. 4. Berry curvature dipole and induced magnetization. (*A*) Sketch of BCD in reciprocal space (green arrows) and magnetization in real space (blue arrows) for + and – chiral structure without electric current. The BCD pattern does not lead to any net magnetization in the absence of an electric current. (*B*) Change of BCD and magnetizations with electric current. The shift of the Fermi surface results in an imbalance of Berry curvature that is associated with a real-space magnetization that can be detected by a magnetized probe. (*C*) (*Upper*) Calculated orbital, spin, and total gyrotropic tensor element K_{zz} as a function of energy near the Fermi level. (*Lower*) Calculated orbital, spin, and total current-induced magnetization $\tilde{\chi}_{zz}$ as a function of energy near the Fermi level. Both K_{zz} and $\tilde{\chi}_{zz}$, which are related by Eq. **2**, are calculated for the chiral structure, and the spin components are exaggerated 20 times. (*D*) Estimated magnetization M_z for two chiral structures using the calculated total $\tilde{\chi}_{zz}$ and the experimental current density J_z. (*E*) Spin-polarized tunneling spectra from two chiral domains (average of +1 and –1mV normalization bias to minimize the uncertainty in tip height). The red and blue curves are obtained above the Co atoms shown as red and blue stars in (*F*), respectively. (*Inset*) Same spectra after removing the chirality-averaged signal, shown as a percentage. (*F*) (*Upper*) SP-STM topography where the spectra are taken. (*Lower*) Color-mapped spin-polarized tunneling spectra across a structural chiral domain boundary (vertical dashed line).

current-induced magnetization M_z constitute pivotal outcomes of this study.

Spin-Sensitive Tunneling Spectroscopy. To verify the behavior of the induced magnetization, we compared the experimental tunneling spectra obtained using a magnetic probe from two chiral domains. The red and blue curves in Fig. 4*E* show the tunneling spectra obtained on top of the Co atoms in opposite chiral domains shown with red and blue stars in Fig. 4*F*, respectively. Since the absolute value of the tunneling current depends on the tip height, we carefully compared spectra taken with normalization biases as low as 1mV to reduce the uncertainty in the height. Fig. 4*E* shows the averaged results between +1 and –1mV normalization bias. The comparison confirmed that the crossing point is located at zero bias within the experimental resolution, with an antisymmetric behavior as in the calculated M_z in Fig. 4*D*. The *Inset* of Fig. 4*E* depicts the difference after removing the chirality-averaged signal with up to 10% of deviation from the average. The detected asymmetry in the tunneling spectra aligns with estimation of the spin polarization in the tunneling current as outlined in *SI Appendix*, Note 4. However, there are still matters to be explored such as a detailed characterization of tip magnetization (45) and or the extent of coupling between orbital angular momentum spin-polarization of the tip (46). We emphasize that, in conventional SP-STM measurements, the crossing points between the opposite magnetic signals usually occur at an arbitrary bias voltage where the dominance of majority and minority spin states changes (2). We consider the zero-bias crossing in our observation to be a critical difference from conventional SP-STM experiments.

Fig. 4 *A* and *B* schematically explain the mechanism of MTE in relation to non-zero BCD. Although the BCD has opposite signs in the opposite chiral structures, that does not induce any net real-space magnetization in the absence of an electric current (Fig. 4*A*), because the positive and negative contributions in k-space cancel each other. However, when a flow of electric current is introduced by tunneling, the shift of the Fermi surface breaks the balance of Berry curvature and leads to a dominance from one side. The + chiral structure has a stronger contribution of positive Berry curvature (Fig. 4 *B*, *Upper*), while the – chiral structure has a more negative contribution (Fig. 4 *B*, *Lower*). The magnetic moments $m_{n\boldsymbol{k},z}$, which follow a similar pattern, result in opposite magnetizations M_z in real space; these can be detected by the magnetized probe through enhanced (parallel magnetizations) or suppressed (antiparallel magnetizations) tunneling probability.

Lastly, we trace the change of the antisymmetric behavior continuously across a domain boundary in Fig. 4*F*. The magnetic tunneling spectra show the atomic corrugation of twelve Co atoms in the path. While the spectral intensity of the left domain is enhanced at negative bias, it is enhanced in the right domain at

positive bias. Again, this antisymmetric behavior indicates that the effect vanishes at zero bias, similar to the other nonequilibrium Berry physics phenomena such as the nonlinear Hall effect (16–20, 47) and the kinetic magnetoelectric effect (12).

Conclusion

We have used SP-STM to demonstrate the detection of crystallographic chirality without long-range magnetic order of Co spins in $Co_{1/3}NbS_2$. By comparing observations made with nonmagnetic and magnetic probes, we have found a change in the magnetic signal across a chiral domain boundary that is correlated with the structural chirality. With the support of comprehensive theoretical calculations, we attribute these observations, which we refer to as a magnetochiral tunneling effect, to the generation of net magnetization and Berry curvature in the region of concentrated current under the tip. The sign reversal of the experimental signal with crystallographic chirality and with the direction of the tunneling current is consistent with a symmetry analysis. From a fundamental point of view, our work highlights that the distributions of Berry curvature and magnetic moments in reciprocal space can manifest themselves as atomic-scale phenomena in real space, while providing, on the practical side, a unique tool that delivers unprecedented resolution in the imaging of chiral domain structures.

Materials and Methods

Crystal Growth. Using the chemical vapor transport reaction method, single crystals of $Co_{1/3}NbS_2$ were grown with iodine serving as a transport agent. A mixture of cobalt powder, niobium powder, and sulfur pieces with a molar ratio of Co:Nb:S=0.7:1:2 was sealed in a quartz tube with iodine under vacuum. (all chemicals are from Alfa Aesar) The sealed quartz tube was placed in a two-zone furnace, where the hot and cold zones were kept at 950 °C and 800 °C, respectively. Crystals with hexagonal shape with a size of a few millimeters were obtained after 4 wk. To confirm the crystal structure, X-ray diffraction on ground powder of the crystals was taken with Cu K_α radiation in a Malvern Panalytical X'Pert 3 powder diffractometer at room temperature.

Transmission Electron Microscopy. Exfoliated sheets of crystals were further thinned by Ar-ion milling and studied using a JEOL-2010F TEM system. Dark-field TEM images were taken with $g_{\pm} = \pm -222$ along the [101] zone axis to obtain the contrast of the chiral crystal structure.

STM. Samples were exfoliated to a few hundred-micron thickness and glued to a Cu–Be sample plate using Epotek H20E conducting epoxy. A metal pin was attached to the top surface using the same epoxy. The assembled sample was transferred to the vacuum chamber of the STM system (USM-1500, Unisoku) and cooled by liquid nitrogen for more than an hour prior to cleaving and transferred to the STM right after the cleaving. Prior to each cleaving, Pt/Ir tips were characterized on Cu(111) and Cr(001) surface for non-magnetic and magnetic experiments, respectively. We used the tip shaping mechanism of Nanonis controller (SPECS) using an indentation with a negative bias toward the metal surfaces, and the dI/dV spectra were subsequently checked. Cr-coated tips were further verified by obtaining layer-by-layer antiferromagnetic contrast from steps on the Cr(001) surface. Once a surface was approached and scanned, we used a coarse moving mechanism to locate a vortex by following a chiral domain boundary. All STM measurements were obtained at liquid nitrogen temperature around 78K (37).

DFT Calculations. First-principles density-functional theory (DFT+U) calculations were performed using the Vienna ab initio simulation package (VASP) within the projected-augmented wave (PAW) framework (48, 49). Nine, eleven, and six valence electrons were included in the PAW pseudopotential of Co, Nb, and S, respectively. We used the PBEsol exchange-correlation functional for solids (50) along with a rotationally invariant implementation of DFT+U (51) to treat the on-site Coulomb correlation effects of the Co 3*d* electrons at the mean-field level. U = 5 eV and J = 1 eV parameters were considered for Co 3*d* states in our DFT+U calculations. These values of the (*U*, *J*) parameters correctly predict the ground state magnetic configuration of $Co_{1/3}NbS_2$ (44). We did not observe any substantial change in the electronic properties on tuning *U* in the 3 to 6 eV range. A non-magnetic configuration was considered in the reported results; however, ferromagnetic and antiferromagnetic orderings yielded similar metallic features with a complex Fermi surface in $Co_{1/3}NbS_2$. A Γ-centered *k* mesh of size 12×12×6 was used to sample the Brillouin zone, and the kinetic energy cutoff of the plane-wave basis set was 650 eV. Structural relaxation was carried out until the residual Hellmann–Feynman forces on each atom were less than 10–4 eV/Å, and the convergence criterion for the electronic self-consistent calculations was 10−8 eV. Both chiral $Co_{1/3}NbS_2$ structures belong to space group $P6_322$ (SG#182) with the DFT+U optimized lattice parameters a = b = 5.692 Å and c = 11.531 Å, which are in good agreement with the previously reported experimental data (44). We refer to the AB structure with Co inner coordinates (1/3, 2/3, 1/4) and (2/3, 1/3, 3/4) as the Chiral +, and the inverted BA structure with Co inner coordinates (2/3, 1/3, 1/4) and (1/3, 2/3, 3/4) as the Chiral – structure. SOC was considered in all DFT+U calculations. The PyProcar package (52) was used for the post-processing of electronic structure data. The WannierBerri package (53) was employed to compute the Berry curvature, Berry curvature dipole, ohmic conductivity, and MTE tensors using the real space tight-binding Hamiltonian generated using Wannier90 (54). The K_{zz}^{orb}, K_{zz}^{spin}, and Berry curvature dipole tensors were computed using a dense k-grid of size 203×203×87 with a broadening width of 100 K. Tests indicate that the results are converged to within ~2% with respect to the k-point sampling. We further utilized a recursive adaptive k-mesh refinement scheme to achieve faster convergence of Berry-curvature-related properties. A relaxation time of $\tau=10^{-12}$ s was adopted.

STM Simulations. The STM simulations toolkit of the GPAW package (55) within the atomic simulation environment (56) was used. The PBE functional (57) with convergence of 4.0×10^{-8} eV^2 / el. for integrated residuals, 5.0×10^{-4} eV for energies, and 10^{-4} electrons/valence electron for electron densities was adopted. The cleaved surface was modeled with four layers of $Co_{1/3}NbS_2$ with a 10 Å vacuum slab. The simulated images were obtained within the Tersoff-Hamann approach (58) with a $2 \times 2 \times 2$ k-point mesh in reciprocal space and a 0.2 Å grid in real space.

Data, Materials, and Software Availability. All study data are included in the article and/or *SI Appendix*.

ACKNOWLEDGMENTS. This work was supported by the W. M. Keck foundation grant to the Keck Center for Quantum Magnetism at Rutgers University. D.V. acknowledges the support from NSF Grant DMR-1954856. S.S. acknowledges the support from the University Research Awards at the University of Rochester.

Author affiliations: [a]Center for Emergent Materials and Department of Physics and Astronomy, Rutgers University, Piscataway, NJ 08854; [b]Department of Mechanical Engineering, University of Rochester, Rochester, NY 14627; [c]Materials Science Program, University of Rochester, Rochester, NY 14627; [d]State Key Laboratory Base of Novel Function Materials and Preparation Science, School of Material Sciences and Chemical Engineering, Ningbo University, Ningbo 315211, China; and [e]Department of Physics and Astronomy, Rutgers University, Piscataway, NJ 08854

1. G. Binnig, H. Rohrer, Scanning tunneling microscopy–From birth to adolescence. *Rev. Mod. Phys.* **59**, 615–625 (1987).
2. R. Wiesendanger, Spin mapping at the nanoscale and atomic scale. *Rev. Mod. Phys.* **81**, 1495–1550 (2009).
3. B. Jäck, Y. Xie, A. Yazdani, Detecting and distinguishing Majorana zero modes with the scanning tunnelling microscope. *Nat. Rev. Phys.* **3**, 541–554 (2021).
4. E. Moreno-Pineda, W. Wernsdorfer, Measuring molecular magnets for quantum technologies. *Nat. Rev. Phys.* **3**, 645–659 (2021).
5. T. Furukawa, Y. Shimokawa, K. Kobayashi, T. Itou, Observation of current-induced bulk magnetization in elemental tellurium. *Nat. Commun.* **8**, 1–5 (2017).
6. V. A. Shalygin, A. N. Sofronov, L. E. Vorob'ev, I. I. Farbshtein, Current-induced spin polarization of holes in tellurium. *Phys. Solid State* **54**, 2362–2373 (2012).

7. T. Yoda, T. Yokoyama, S. Murakami, Current-induced orbital and spin magnetizations in crystals with helical structure. *Scientific Rep.* **5**, 1–7 (2015).
8. Y. Nabei *et al.*, Current-induced bulk magnetization of a chiral crystal CrNb3S6. *Appl. Phys. Lett.* **117**, 052408 (2020).
9. A. Inui *et al.*, Chirality-induced spin-polarized state of a chiral crystal CrNb3S6. *Phys. Rev. Lett.* **124**, 166602 (2020).
10. F. Calavalle *et al.*, Gate-tuneable and chirality-dependent charge-to-spin conversion in tellurium nanowires. *Nat. Mater.* **21**, 526–532 (2022).
11. S. Zhong, J. E. Moore, I. Souza, Gyrotropic magnetic effect and the magnetic moment on the fermi surface. *Phys. Rev. Lett.* **116**, 077201 (2016).
12. S. S. Tsirkin, P. A. Puente, I. Souza, Gyrotropic effects in trigonal tellurium studied from first principles. *Phys. Rev. B* **97**, 035158 (2018).
13. G. Gatti *et al.*, Radial spin texture of the Weyl fermions in chiral tellurium. *Phys. Rev. Lett.* **125**, 216402 (2020).
14. D. Hara, M. S. Bahramy, S. Murakami, Current-induced orbital magnetization in systems without inversion symmetry. *Phys. Rev. B* **102**, 184404 (2020).
15. C. Şahin, J. Rou, J. Ma, D. A. Pesin, Pancharatnam–Berry phase and kinetic magnetoelectric effect in trigonal tellurium. *Phys. Rev. B* **97**, 205206 (2018).
16. Z. Z. Du, C. M. Wang, H.-P. Sun, H.-Z. Lu, X. C. Xie, Quantum theory of the nonlinear Hall effect. *Nat. Commun.* **12**, 5038 (2021).
17. I. Sodemann, L. Fu, Quantum nonlinear Hall effect induced by berry curvature dipole in time-reversal invariant materials. *Phys. Rev. Lett.* **115**, 216806 (2015).
18. J. E. Moore, J. Orenstein, Confinement-induced Berry phase and helicity-dependent photocurrents. *Phys. Rev. Lett.* **105**, 026805 (2010).
19. J. Son, K.-H. Kim, Y. H. Ahn, H.-W. Lee, J. Lee, Strain engineering of the Berry curvature dipole and valley magnetization in monolayer MoS_2. *Phys. Rev. Lett.* **123**, 036806 (2019).
20. S. Singh, J. Kim, K. M. Rabe, D. Vanderbilt, Engineering Weyl phases and nonlinear Hall effects in Td-$MoTe_2$. *Phys. Rev. Lett.* **125**, 046402 (2020).
21. Y. M. Itahashi *et al.*, Giant second harmonic transport under time-reversal symmetry in a trigonal superconductor. *Nat. Commun.* **13**, 1659 (2022).
22. N. B. Baranova, Yu. V. Bogdanov, B. Ya. Zel'Dovich, Electrical analog of the Faraday effect and other new optical effects in liquids. *Opt. Commun.* **22**, 243–247 (1977).
23. V. M. Edelstein, Spin polarization of conduction electrons induced by electric current in two-dimensional asymmetric electron systems. *Solid State Commun.* **73**, 233–235 (1990).
24. S.-Y. Xu *et al.*, Electrically switchable Berry curvature dipole in the monolayer topological insulator WTe_2. *Nat. Phys.* **14**, 900–906 (2018).
25. S. Sinha *et al.*, Berry curvature dipole senses topological transition in a Moiré superlattice. *Nat. Phys.* **18**, 765–770 (2022).
26. K.-H. Jin, E. Oh, R. Stania, F. Liu, H. W. Yeom, Enhanced Berry curvature dipole and persistent spin texture in the Bi(110) monolayer. *Nano Lett.* **21**, 9468–9475 (2021).
27. L. Du *et al.*, Engineering symmetry breaking in 2D layered materials. *Nat. Rev. Phys.* **3**, 193–206 (2021).
28. S.-W. Cheong, S. Lim, K. Du, F.-T. Huang, Permutable SOS (symmetry operational similarity). *npj Quant. Mater.* **6**, 1–10 (2021).
29. K. Du *et al.*, Topological spin/structure couplings in layered chiral magnet Cr1/3TaS2: The discovery of spiral magnetic superstructure. *Proc. Natl. Acad. Sci. U.S.A.* **118**, e2023337118 (2021).
30. Y. Horibe *et al.*, Color theorems, chiral domain topology, and magnetic properties of FexTaS2. *J. Am. Chem. Soc.* **136**, 8368–8373 (2014).
31. S. Lim *et al.*, Tunable single-atomic charges on a cleaved intercalated transition metal dichalcogenide. *Nano Lett.* **22**, 1812–1817 (2022).
32. S.-W. Cheong, SOS: Symmetry-operational similarity. *npj Quant. Mater.* **4**, 1–9 (2019).
33. S. Dalum, P. Hedegård, Theory of chiral induced spin selectivity. *Nano Lett.* **19**, 5253–5259 (2019).
34. T. Yoda, T. Yokoyama, S. Murakami, Orbital Edelstein effect as a condensed-matter analog of solenoids. *Nano Lett.* **18**, 916–920 (2018).
35. H. D. Flack, Chiral and achiral crystal structures. *Helv. Chim. Acta* **86**, 905–921 (2003).
36. F.-T. Huang, S.-W. Cheong, Aperiodic topological order in the domain configurations of functional materials. *Nat. Rev. Mater.* **2**, 17004 (2017).
37. S. Lim *et al.*, Magnetochiral spin-polarized tunneling in a paramagnetic state (2021). https://doi.org/10.21203/rs.3.rs-70373/v1. Accessed 2 December 2021.
38. S. S. P. Parkin, E. A. Marseglia, P. J. Brown, Magnetic structure of Co1/3NbS2 and Co1/3TaS2. *J. Phys. C: Solid State Phys.* **16**, 2765 (1983).
39. G. Tenasini *et al.*, Giant anomalous Hall effect in quasi-two-dimensional layered antiferromagnet Co1/3NbS2. *Phys. Rev. Res.* **2**, 023051 (2020).
40. N. J. Ghimire *et al.*, Large anomalous Hall effect in the chiral-lattice antiferromagnet CoNb3S6. *Nat. Commun.* **9**, 3280 (2018).
41. S. S. P. Parkin, E. A. Marseglia, P. J. Brown, Magnetic structure of Co1/3NbS2 and Co1/3TaS2. *J. Phys. C: Solid State Phys.* **16**, 2765–2778 (1983).
42. N. Zhang *et al.*, Magnetotransport signatures of Weyl physics and discrete scale invariance in the elemental semiconductor tellurium. *Proc. Natl. Acad. Sci. U.S.A.* 117, 11337–11343 (2020).
43. J. Xiao *et al.*, Berry curvature memory through electrically driven stacking transitions. *Nat. Phys.* **16**, 1028–1034 (2020).
44. P. Popčević *et al.*, Electronic transport and magnetism in the alternating stack of metallic and highly frustrated magnetic layers in Co1/3NbS2. *Phys. Rev. B* **107**, 235149 (2023).
45. M. Enayat *et al.*, Real-space imaging of the atomic-scale magnetic structure of Fe1+yTe. *Science* **345**, 653–656 (2014).
46. Y. Xing *et al.*, Localized spin–orbit polaron in magnetic Weyl semimetal Co3Sn2S2. *Nat. Commun.* **11**, 5613 (2020).
47. Q. Ma *et al.*, Observation of the nonlinear Hall effect under time-reversal-symmetric conditions. *Nature* **565**, 337–342 (2019).
48. G. Kresse, J. Furthmüller, Efficient iterative schemes for ab initio total-energy calculations using a plane-wave basis set. *Phys. Rev. B* **54**, 11169–11186 (1996).
49. G. Kresse, D. Joubert, From ultrasoft pseudopotentials to the projector augmented-wave method. *Phys. Rev. B* **59**, 1758–1775 (1999).
50. J. P. Perdew *et al.*, Restoring the density-gradient expansion for exchange in solids and surfaces. *Phys. Rev. Lett.* **100**, 136406 (2008).
51. A. I. Liechtenstein, V. I. Anisimov, J. Zaanen, Density-functional theory and strong interactions: Orbital ordering in Mott–Hubbard insulators. *Phys. Rev. B* **52**, R5467–R5470 (1995).
52. U. Herath *et al.*, PyProcar: A Python library for electronic structure pre/post-processing. *Comput. Phys. Commun.* **251**, 107080 (2020).
53. S. S. Tsirkin, High performance Wannier interpolation of Berry curvature and related quantities with WannierBerri code. *npj Comput. Mater* **7**, 1–9 (2021).
54. A. A. Mostofi *et al.*, wannier90: A tool for obtaining maximally-localised Wannier functions. *Comput. Phys. Commun.* **178**, 685–699 (2008).
55. J. J. Mortensen, L. B. Hansen, K. W. Jacobsen, Real-space grid implementation of the projector augmented wave method. *Phys. Rev. B* **71**, 035109 (2005).
56. A. H. Larsen *et al.*, The atomic simulation environment–A Python library for working with atoms. *J. Phys.: Condens. Matter* **29**, 273002 (2017).
57. J. P. Perdew, K. Burke, M. Ernzerhof, Generalized gradient approximation made simple. *Phys. Rev. Lett.* **77**, 3865–3868 (1996).
58. J. Tersoff, D. R. Hamann, Theory of the scanning tunneling microscope. *Phys. Rev. B* **31**, 805–813 (1985).